




Gate-tunable topological phases in superlattice modulated bilayer graphene

Yongxin Zeng ^{1,2,3}, Tobias M. R. Wolf,³ Chunli Huang,⁴ Nemin Wei ^{3,5}, Sayed Ali Akbar Ghorashi,⁶
Allan H. MacDonald,³ and Jennifer Cano ^{2,6}

¹*Department of Physics, Columbia University, New York 10027, New York*

²*Center for Computational Quantum Physics, Flatiron Institute, New York 10010, New York*

³*Department of Physics, University of Texas at Austin, Austin 78712, Texas*

⁴*Department of Physics and Astronomy, University of Kentucky, Lexington 40506-0055, Kentucky*

⁵*Department of Physics, Yale University, New Haven 06520, Connecticut*

⁶*Department of Physics and Astronomy, Stony Brook University, Stony Brook 11794, New York*



(Received 17 January 2024; revised 7 April 2024; accepted 12 April 2024; published 2 May 2024)

Superlattice potential modulation can produce flat minibands in Bernal-stacked bilayer graphene. In this work we study how band topology and interaction-induced symmetry-broken phases in this system are controlled by tuning the displacement field and the shape and strength of the superlattice potential. We use an analytic perturbative analysis to demonstrate that topological flat bands are favored by a honeycomb-lattice-shaped potential, and numerics to show that the robustness of topological bands depends on both the displacement field strength and the periodicity of the superlattice potential. At integer fillings of the topological flat bands, the strength of the displacement field and the superlattice potential tune phase transitions between quantum anomalous Hall insulator, trivial insulator, and metallic states. We present mean-field phase diagrams in a gate voltage parameter space at filling factor $\nu = 1$, and discuss the prospects of realizing quantum anomalous Hall insulators and fractional Chern insulators when the superlattice potential modulation is produced by dielectric patterning or adjacent moiré materials.

DOI: [10.1103/PhysRevB.109.195406](https://doi.org/10.1103/PhysRevB.109.195406)

I. INTRODUCTION

Moiré materials including twisted graphene [1–10] and transition metal dichalcogenide (TMD) [11–24] heterostructures have attracted a tremendous amount of research interest. Motivated by the rich phenomenology observed in moiré materials, alternate flat-band platforms [25–30] have been proposed. Topological flat-band systems are especially interesting as the interplay between correlation and topology leads to quantum anomalous Hall [5,18] and fractional Chern insulators [6,10,21–23] at integer and fractional fillings, respectively. Flat bands with nonzero Chern numbers are reminiscent of Landau levels in quantum Hall systems [31–36], and could underlie many of the exotic phenomena observed in moiré materials, including superconductivity [37–39].

Recent experimental advances have enabled creation of artificial superlattices by the gate-patterning technique [40–46] or by adjacent moiré materials [47–53], and the physical consequences have been discussed [26,27,54–62]. In particular, it was shown in a recent study [26] that Bernal stacked bilayer graphene modulated by a superlattice potential (SL-BLG) provides a versatile platform for the study of flat-band physics. Band structure calculations show that SL-BLG hosts topologically nontrivial flat bands under weak superlattice potential modulation, and a stack of trivial flat bands under strong modulation. The flat bands in different parameter regimes are reminiscent of those in graphene and TMD moiré materials, but the high tunability makes SL-BLG a unique platform for the study of correlated and topological phases.

Despite the discovery of topological flat bands in SL-BLG in a large parameter regime, the origin of these topological flat bands is not clear. Multiple band inversions in parameter space lead to rich but complicated band structure and topology. In this paper we show that the topology of the lowest bands is robust at least in the weak modulation regime; when the superlattice potential is weak compared to the displacement field, the lowest miniband above charge neutrality is always topologically nontrivial when the superlattice potential minima form a honeycomb lattice. We further perform mean-field calculations at filling factor $\nu \equiv NA_0/A = 1$ of the topological flat bands and find that the system is a valley-polarized quantum anomalous Hall insulator over a large parameter range. (Here N is the number of electrons, A is the area of the system, and A_0 is the area of one unit cell.)

This paper is organized as follows. In Sec. II, we introduce our model system and show how its band structure and topology is influenced by the strength of displacement field and the shape of superlattice potential. In Sec. III, we study interaction effects at filling $\nu = 1$ of the topological flat bands and present mean-field phase diagrams. Finally, we conclude our work in Sec. IV with a discussion of the prospects for experimental realization of quantum anomalous Hall and fractional Chern insulators within the SL-BLG platform.

II. BAND TOPOLOGY

A. Model

We consider a SL-BLG. For concreteness, we consider the experimental setup shown in Fig. 1 in which the superlattice potential is produced by a periodic pattern on the

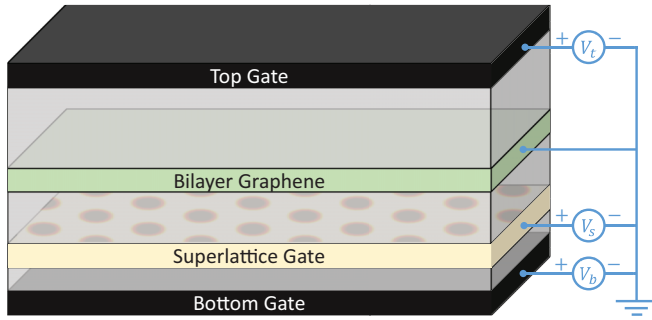


FIG. 1. Schematic illustration of the SL-BLG device structure. The top and bottom gate voltages V_t , V_b control the net charge density on bilayer graphene and the displacement field strength, while the superlattice gate voltage V_s controls the superlattice potential strength. The gray regions represent dielectric layers that separate the active layers from the gates.

superlattice gate. The gate-patterning technique depicted in Fig. 1 has been demonstrated in recent experiments [40–46] and in principle allows superlattice potentials of arbitrary shapes and periodicities. By tuning the top and bottom gate voltages V_t , V_b and the superlattice gate voltage V_s , the net charge density, displacement field, and superlattice potential strength can be independently controlled. We note that another efficient method to impose a superlattice potential is by including a twisted hexagonal boron nitride (hBN) bilayer, which exhibits a spatially periodic pattern of out-of-plane electric polarizations [47–50], in the van der Waals layer stack. A doped TMD moiré bilayer with localized charge carriers [51–53] is yet another possibility, but for a general theoretical discussion we focus first on the highly tunable device structure in Fig. 1 and defer the discussion of hBN and TMD bilayers to Sec. IV.

The system is described by the Hamiltonian

$$H = H_{\text{BLG}} + H_{\text{SL}} + H_{\text{int}}. \quad (1)$$

Here H_{BLG} is the Hamiltonian for bilayer graphene (BLG) with a displacement field [63]:

$$H_{\text{BLG}} = \sum_{\tau s k} \Psi_{\tau s k}^\dagger \left[\hbar v (\tau k_x \sigma_1 + k_y \sigma_2) + \frac{t}{2} (\rho_1 \sigma_1 - \rho_2 \sigma_2) + V_0 \rho_3 \right] \Psi_{\tau s k}, \quad (2)$$

where $\tau = \pm$ and $s = \uparrow, \downarrow$ are the valley and spin labels, Ψ is a four-component spinor with layer and sublattice components, and ρ and σ are, respectively, layer and sublattice Pauli matrices, $v = 10^6$ m/s is the Dirac velocity, $t = 0.4$ eV is the dominant interlayer hopping amplitude, and V_0 is the displacement field strength. Trigonal warping terms are neglected as in Ref. [26]. While trigonal warping plays a crucial role for the nature of correlated metallic states in bilayer and trilayer graphene in the limit of zero superlattice potential and low carrier densities [64–70], its effect is unimportant when a superlattice potential stronger than the energy scale associated with trigonal warping (which is typically ~ 1 meV) is present and dominates the physics of correlated states, which is the parameter regime of interest to this work. H_{SL} describes the

superlattice potential modulation:

$$H_{\text{SL}} = \sum_{\tau s} \int d\mathbf{r} \Psi_{\tau s}^\dagger(\mathbf{r}) V(\mathbf{r}) \Psi_{\tau s}(\mathbf{r}). \quad (3)$$

In this paper we focus on triangular superlattice potentials. To lowest order in the Fourier expansion,

$$V(\mathbf{r}) = \left(\frac{1 + \alpha}{2} \rho_0 + \frac{1 - \alpha}{2} \rho_3 \right) \left(\sum_{n=0}^2 V_{\text{SL}} e^{i\mathbf{g}_n \cdot \mathbf{r}} + \text{c.c.} \right), \quad (4)$$

where in general $V_{\text{SL}} = |V_{\text{SL}}| e^{i\phi}$ is a complex parameter, and $\mathbf{g}_n = (4\pi/\sqrt{3}L)(\cos(2n\pi/3), \sin(2n\pi/3))$ with $n = 0, 1, 2$ are reciprocal lattice vectors of the triangular superlattice with lattice constant L . The phase ϕ determines the ratios of the superlattice potential values at three high-symmetry points within a unit cell; they are, respectively, proportional to $\cos \phi$, $\cos(\phi + 2\pi/3)$, and $\cos(\phi - 2\pi/3)$. The lower two become degenerate at $\phi = 2n\pi/3$ and at this point the potential minima form a honeycomb lattice. Similarly the potential maxima form a honeycomb lattice when $\phi = (2n + 1)\pi/3$. $\alpha \in (0, 1)$ is the ratio of effective superlattice potential strengths felt by the top and bottom graphene layers. In this paper we choose $\alpha = 0.9$. Note that the value of α here is its *bare* value that only accounts for the geometric origin of layer asymmetry, i.e., the fact that the bottom layer is closer to the superlattice gate than the top layer. Electrostatic screening leads to a much reduced effective α [71], but this effect is taken into account self-consistently by our Hartree-Fock calculations. To avoid double-counting, we start with a large bare α in the single-particle Hamiltonian. The precise value of α does not qualitatively affect our results.

The last term in Eq. (1) is the Coulomb interaction

$$H_{\text{int}} = \frac{1}{2A} \sum_{l'l'q} V_{l'l'}(q) : n_{l,q} n_{l',-q} :, \quad (5)$$

where $n_{l,q} = \sum_{\sigma\tau s k} a_{l\sigma\tau s, k+q}^\dagger a_{l\sigma\tau s, k}$ is the density operator in layer l , $V_{l'l'}(q) = 2\pi e^2/\epsilon q$ for $l = l'$ and $V_{l'l'}(q) = (2\pi e^2/\epsilon q) e^{-qd}$ for $l \neq l'$ where ϵ is the dielectric constant and d is the distance between the two graphene layers. The colons represent normal ordering of creation and annihilation operators. In our calculations we take $\epsilon = 10$ and $d = 3.5$ Å. Intralayer and interlayer interactions must be distinguished in order to account for screening effects properly. Our calculations also account for gate-screening effects that are discussed in the Appendix.

The Chern number of an isolated energy band (labeled by n) is defined as [72] the integral of Berry curvature in the mini Brillouin zone (mBZ) of the long-period superlattice:

$$C_n = \frac{1}{2\pi} \int_{\text{mBZ}} d^2\mathbf{k} \Omega_{n,\mathbf{k}}, \quad (6)$$

with Berry curvature

$$\Omega_{n,\mathbf{k}} = i \left(\langle \partial_{k_x} u_{n\mathbf{k}} | \partial_{k_y} u_{n\mathbf{k}} \rangle - \langle \partial_{k_y} u_{n\mathbf{k}} | \partial_{k_x} u_{n\mathbf{k}} \rangle \right), \quad (7)$$

where $|u_{n\mathbf{k}}\rangle$ is the Bloch eigenstate of band n .

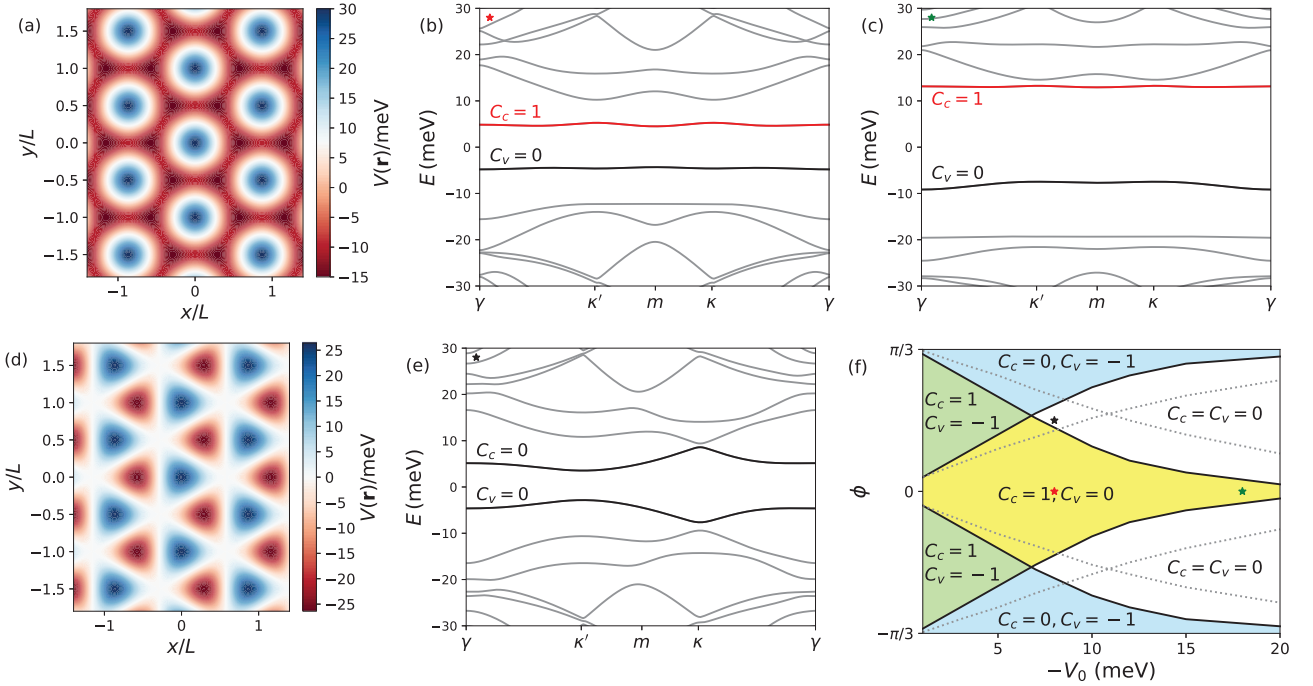


FIG. 2. Band structure and topology of SL-BLG. (a) Superlattice potential with $|V_{\text{SL}}| = 5$ meV and $\phi = 0$. The potential minima form a honeycomb lattice and the potential maxima form a triangular lattice. (b),(c) Band structure in valley $\tau = -1$ with displacement field (b) $V_0 = -8$ meV (c) $V_0 = -18$ meV, with the superlattice potential in (a) and lattice constant $L = 50$ nm. (d),(e) Same plots as in (a),(b) but with $\phi = \pi/6$. (f) Topological phase diagram in V_0 - ϕ parameter space with fixed $|V_{\text{SL}}| = 5$ meV. C_c and C_v are the valley-projected Chern numbers of the first conduction and valence minibands respectively. The Chern numbers of the corresponding bands in the other valley are equal and opposite, leading to zero net Chern number when both valleys are included. The colored regions separated by solid lines represent different topological phases for $L = 50$ nm, while the dotted lines are phase boundaries for $L = 30$ nm. The red, green, and black stars represent the parameter choices in (b), (c), and (e), respectively.

B. Band structure and topology

The electronic band structure of SL-BLG has been studied in detail in Ref. [26]. Here, we briefly review some results and provide new insight into the nature of topological flat bands.

In the absence of a superlattice potential, a displacement field opens a $2|V_0|$ gap. The result is a valley Hall insulator with nonzero Berry curvature concentrated near the conduction band bottom and valence band top in each valley. With a weak superlattice potential ($|V_{\text{SL}}| \ll |V_0|$), the conduction band electrons are localized near the potential minima and the valence band holes near the potential maxima. The potential minima form a triangular lattice for generic phase angles $\phi = \arg V_{\text{SL}}$, but two local minima become degenerate at $\phi = 2n\pi/3$ and together form a honeycomb lattice [Fig. 2(a)]. Similarly, the potential maxima form a honeycomb lattice near $\phi = (2n+1)\pi/3$ and a triangular lattice otherwise. We show below that lattice geometry is crucial for the topological properties of low-energy minibands; topological bands are favored by honeycomb lattices while triangular lattices are likely to host trivial bands.

Below we focus on the first miniband above charge neutrality. Physically this band represents the lowest bound state of conduction band electrons localized near the superlattice potential minima. Because the band dispersion of BLG is flat near the band extrema, the bandwidth of the first conduction miniband is small even with relatively weak potential modulation. To understand the topology of the band, we assume a

weak superlattice potential and perform degenerate state perturbation theory near the κ point [$\kappa = (2\pi/3L)(\sqrt{3}, 1)$] of the mBZ. Folding the conduction band into the first mBZ, the lowest energy level at κ is threefold degenerate. The superlattice potential couples these three states and lifts the degeneracy. Projecting the superlattice potential onto the 3×3 low-energy subspace, the Hamiltonian matrix reads

$$H_\kappa = \begin{pmatrix} E_\kappa & V_\kappa & V_\kappa^* \\ V_\kappa^* & E_\kappa & V_\kappa \\ V_\kappa & V_\kappa^* & E_\kappa \end{pmatrix}, \quad (8)$$

where E_κ is the conduction band energy at κ and $V_\kappa = \langle \kappa | V | \kappa - \mathbf{g}_0 \rangle$ is the superlattice potential projected onto the low-energy subspace. If the basis states were trivial plane waves, $V_\kappa = V_{\text{SL}}$ would simply be the Fourier coefficient of the superlattice potential. However, the BLG basis states have nontrivial spinor structures which produce an extra phase factor $e^{i\phi}$, i.e., $\arg V_\kappa = \phi + \phi'$. A similar analysis applies for the bands at $\kappa' = -\kappa$, but here the projected matrix element has the phase angle $\arg V_{\kappa'} = \phi - \phi'$.

The matrix H_κ has three distinct eigenvalues in general, but the lower two eigenvalues become degenerate when $\arg V_\kappa = 2n\pi/3$. At this point the lower two bands form a Dirac cone near κ . By a similar argument the gap closes at κ' when $\arg V_{\kappa'} = 2n\pi/3$. For a trivial band without any internal spinor structure, $\phi' = 0$, the gap closes simultaneously at κ

and κ' and the band topology does not change. In this case the lowest band is topologically trivial for any $\phi \neq 2n\pi/3$. When $\phi' \neq 0$, the gap closes at $\phi = 2n\pi/3 - \phi'$ at κ and $\phi = 2n\pi/3 + \phi'$ at κ' , opening up an interval $\phi \in (2n\pi/3 - \phi', 2n\pi/3 + \phi')$ within which the lowest band is topologically nontrivial. The point $\phi = 2n\pi/3$ at which the potential minima form a honeycomb lattice is at the middle of the topological region and is the optimal parameter choice for a topological flat band. This explains why in Ref. [26] [see also Figs. 2(a)–2(c)], where $\phi = 0$ is implicitly assumed, the first miniband above charge neutrality is topologically nontrivial, while the band below, which originates from valence band holes localized at the potential maxima that form a triangular lattice, is topologically trivial.

The phase ϕ' originates from the nontrivial geometry of Bloch wave functions and determines the width of the topological region. Roughly speaking ϕ' is proportional to the Berry flux of the conduction band within the first mBZ. For small ϕ' , gap closings at κ and κ' occur almost simultaneously as ϕ varies. While the lowest miniband is topologically nontrivial between these two gap closings, it is separated from the second lowest band only by a very small gap. For BLG, this is the case when the displacement field V_0 is large such that the Bloch wave functions near the conduction band bottom have little winding [see Fig. 2(c)]. In order to obtain an isolated topological flat band, V_0 cannot be too large. An approximate criterion, obtained by requiring a significant amount of Berry flux within the first mBZ, is that $V_0 \lesssim (\hbar^2 v^2 / t)(2\pi/L)^2$. A smaller lattice constant L implies a larger mBZ which contains a larger amount of Berry flux and therefore a larger ϕ' and a wider topological region.

Figure 2(f) shows the phase diagram in V_0 - ϕ parameter space with fixed $|V_{SL}| = 5$ meV. In agreement with the above discussion, the topological region is centered at $\phi = 0$ for the first conduction miniband and $\phi = \pi/3$ for the first valence miniband, and the width of the topological region shrinks rapidly with increasing $|V_0|$. The topological region becomes wider at smaller lattice constant L , as is clear from the comparison between the $L = 50$ nm (solid lines) and $L = 30$ nm (dotted lines) phase boundaries.

As the superlattice potential strength $|V_{SL}|$ increases, the conduction minibands move down and the valence minibands move up. The conduction and valence minibands start to mix when $|V_{SL}| \sim V_0$ and above this point the band structure becomes complicated and sensitive to parameters. In the strong modulation limit the system becomes a quantum dot array with electrons and holes confined in neighboring sites. In this paper, we focus on the regime of relatively weak superlattice potential in which the band structure and topology can be understood by the arguments above, and leave the study of the strong modulation limit to future work.

III. CORRELATED STATES IN SL-BLG

In this section we study correlated states in SL-BLG at partial filling of the minibands, with emphasis on the topology of correlated insulating states. Since topological bands are favored by honeycomb lattices, we choose $\phi = 0$ and focus on the first conduction miniband. The effects of varying ϕ will also be discussed.

A. Mean-field theory

We study interaction effects by Hartree-Fock mean-field theory. Because the first conduction miniband is not flat and isolated for generic parameters V_0 and V_{SL} , we do not project interactions onto the low-energy minibands, but instead perform mean-field calculations in the plane-wave basis. The mean-field Hamiltonian consists of single-particle terms and Hartree-Fock self-energies:

$$H_{MF} = H_{BLG} + H_{SL} + \Sigma_H + \Sigma_F. \quad (9)$$

The Hartree term is physically an electrostatic potential:

$$\Sigma_H = \frac{1}{A} \sum_{l\sigma\tau s} \sum_{\mathbf{g}\mathbf{k}} \left[\sum_{l'} V_{ll'}(\mathbf{g}) n_{l'g} \right] a_{l\sigma\tau s, \mathbf{k}+\mathbf{g}}^\dagger a_{l\sigma\tau s, \mathbf{k}}, \quad (10)$$

where $n_{lg} = \sum_{\sigma\tau sk} \langle a_{l\sigma\tau s, \mathbf{k}-\mathbf{g}}^\dagger a_{l\sigma\tau s, \mathbf{k}} \rangle$ is the Fourier transform of electron density in layer l . The Hartree potential must be regularized because of the negative energy sea; we account for its effects by defining $\langle \dots \rangle$ in the self-consistent field equations as the expectation value in the mean-field ground state subtracted by that in charge-neutral BLG in the absence of external fields. The Fock term is

$$\begin{aligned} \Sigma_F = & -\frac{1}{A} \sum_{l'\sigma'\tau's'} \sum_{l\sigma\tau s} \sum_{\mathbf{k}\mathbf{k}'} V_{ll'}(\mathbf{k}' - \mathbf{k} - \mathbf{g}) \\ & \times \langle a_{l\sigma\tau s, \mathbf{k}'-\mathbf{g}}^\dagger a_{l'\sigma'\tau's', \mathbf{k}'} \rangle a_{l'\sigma'\tau's', \mathbf{k}+\mathbf{g}}^\dagger a_{l\sigma\tau s, \mathbf{k}}. \end{aligned} \quad (11)$$

In Eqs. (10) and (11) we have assumed that the translational symmetry of the superlattice is preserved. The mean-field ground state is obtained by solving the mean-field equations self-consistently. The Berry curvature and Chern number of mean-field energy bands are given by the same expressions in Eqs. (6) and (7), but with the single-particle Bloch eigenstates replaced by the self-consistent mean-field eigenstates.

B. Phase diagrams

The single-particle band structure has four-fold spin-valley degeneracy. Therefore at miniband filling $\nu = 1$, the first conduction miniband of each flavor is quarter-filled, resulting in a metallic state, when interactions are absent. This is indeed the case when the superlattice potential is weak so that the minibands remain dispersive. As the first miniband flattens with increasing $|V_{SL}|$, it is energetically favorable to form a correlated insulating state by spontaneously breaking the spin-valley degeneracy. The threshold $|V_{SL}|$ for correlated insulating states decreases with $|V_0|$ because increasing $|V_0|$ flattens the BLG bands. Interestingly, at large $|V_0|$ the correlated insulating state persists to the limit of vanishing $|V_{SL}|$, pointing to the possibility of Wigner crystallization in BLG at large displacement field and low carrier density [73]. The possibility of Wigner crystallization in BLG has been studied theoretically in Refs. [74,75]. Experimental signatures of an insulating state in BLG have been observed [66] at low carrier density and large displacement field and are interpreted as evidence of spontaneous crystallization. A careful study of Wigner crystallization in BLG needs to take into account trigonal warping effects and to consider a range of carrier densities, which is outside the scope of the current work.

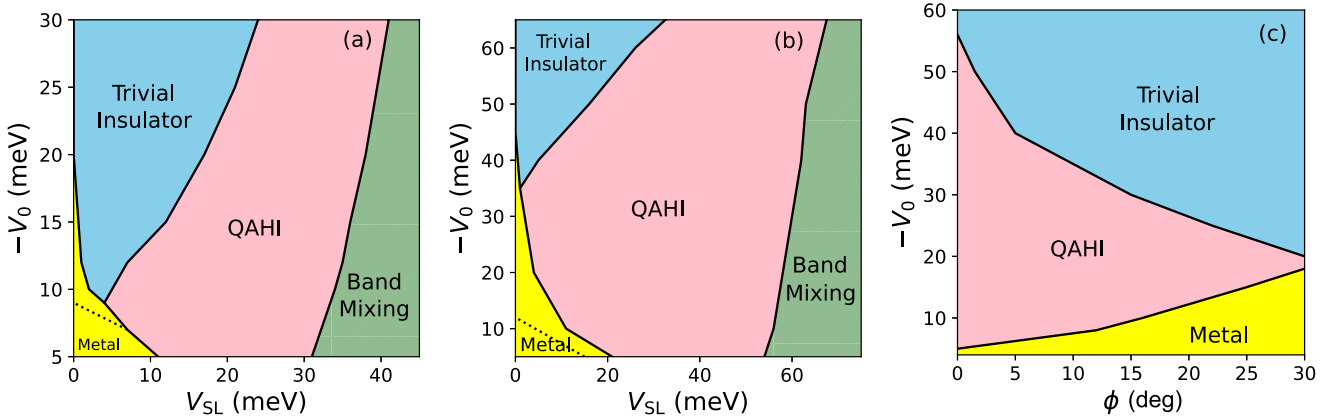


FIG. 3. Mean-field phase diagrams at filling factor $\nu = 1$. (a) and (b) are phase diagrams in displacement field V_0 and superlattice potential strength $|V_{SL}|$ plane, with fixed $\phi = 0$ but different lattice constants: (a) $L = 50$ nm; (b) $L = 30$ nm. The dotted lines in the yellow regions separate the time-reversal-symmetric metallic states on the lower left and the valley-imbalanced metallic states (anomalous Hall metal) on the upper right. The band mixing (hatched green) regions identify large- $|V_{SL}|$ semimetal states in which conduction and valence minibands overlap and mix, leading to a complicated series of phase transitions between insulating and metallic states that we do not study in detail in this work. (c) is the phase diagram in V_0 and ϕ at fixed $|V_{SL}| = 20$ meV and $L = 30$ nm. Here all metallic states break time-reversal symmetry.

A more careful examination of the metallic states shows that at large $|V_0|$ and $|V_{SL}|$, the metallic state is spontaneously valley-imbalanced, breaking time-reversal symmetry. Because of the opposite Berry curvatures in the two valleys of BLG, such a metallic state is expected to show an anomalous Hall effect. The transition from such anomalous Hall metal state to insulating states occurs via a continuous closing of an indirect band gap while the transition from the time-reversal symmetric metallic state to the quantum anomalous Hall insulator (QAH) is a first-order transition.

In our mean-field calculations we find that spin-valley-polarized states are energetically favored over intervalley-coherent states. The topological properties of these correlated insulating states, however, depend on the system parameters. If the only relevant band is the first conduction miniband and the shape parameter of the superlattice potential is near $\phi = 0$, spin and valley polarized insulating states are QAHI with net Chern number $|C| = 1$. This is the case when the first conduction miniband is isolated from all other bands by a gap larger than the interaction energy scale. According to the discussion in the last section, at $\phi = 0$ the first conduction miniband is flat and isolated only at intermediate values of $|V_0|$ and $|V_{SL}|$. At large $|V_0|$ the gap between the first and second minibands is small, and the Berry curvature is strongly localized near the κ and κ' points. At large $|V_{SL}|$, on the other hand, mixing between the conduction and valence minibands becomes important, and the first conduction miniband is generally not flat or isolated.

The above picture is confirmed by the mean-field phase diagrams in Fig. 3. We find that the ground state at filling $\nu = 1$ is a QAHI over a large region in voltage parameter space. At small $|V_0|$ the system is metallic at small $|V_{SL}|$ and becomes a QAHI above a threshold $|V_{SL}|$. The QAHI state persists until the conduction and valence minibands mix at large $|V_{SL}|$, after which the system becomes either a trivial insulator or a metal. The phase diagram in the semimetal-like conduction/valence band-mixing regime (hatched green region in Fig. 3) at large $|V_{SL}|$ is mostly topologically trivial.

Flavor symmetry breaking properties in this regime are highly sensitive to parameters, and in all likelihood not predicted correctly by Hartree-Fock theory. As $|V_0|$ increases, mixing between the first and second conduction minibands becomes increasingly important and leads to the emergence of a trivial insulating state with net Chern number $C = 0$ between the metallic and QAH states at large $|V_0|$. Both insulating states are valley-polarized and break time-reversal symmetry, and the transition between them occurs via a continuous gap closing. The trivial insulator region expands with increasing $|V_0|$, accompanied by the shrinking of the QAHI region.

Figures 3(a) and 3(b) are phase diagrams at different lattice constants L . Comparison of the two shows that the QAHI region is significantly larger at smaller L . This is consistent with the single-particle phase diagram in Fig. 2(e) in which the topological region widens at large L . Figure 3(c) shows that the QAHI region quickly narrows as ϕ increases from 0 to $\pi/6$, in agreement with the insight from the last section that topological bands are favored by honeycomb lattices ($\phi = 0$).

IV. CONCLUSION AND DISCUSSION

In this paper we studied the band structure and topology of SL-BLG as well as correlated insulating states that appear at partial filling of the first conduction miniband. We found that the ground state at filling $\nu = 1$ is a spin-valley-polarized QAHI when the first conduction miniband is isolated, flat, and topologically nontrivial. According to the analysis in Sec. II, this is the case when: (i) the superlattice potential minima form a honeycomb lattice with two equivalent sublattices (i.e., $\phi = 0$); and (ii) the displacement field V_0 and superlattice potential strength $|V_{SL}|$ are relatively weak. The large stable QAHI regions in our mean-field phase diagrams (Fig. 3) suggest that QAHI should be routinely realized in honeycomb-superlattice potential modulated BLG with no need for fine tuning.

Our gap-closing argument in Sec. II is not specific to BLG; generalization to other systems as well as other

superlattice geometries is straightforward. We note that similar perturbative analysis was performed in Refs. [55–58,76] in different contexts but with qualitatively similar results. Our argument shows that when weak honeycomb-lattice potential modulation is applied to any gapped system with nontrivial band geometry, the lowest miniband above the band gap is likely to be topologically nontrivial. Since the central point of our argument is built upon Berry phase effects that break the effective time-reversal symmetry of the single-valley Hamiltonian and gap out the Dirac cones at κ, κ' , our results are also applicable to kagome lattice potential modulations. Note, however, that gap closing at $\boldsymbol{\gamma} = (0, 0)$ and $\boldsymbol{m} = (2\pi/\sqrt{3}L, 0)$ can also change the topology of minibands. Neither case occurs in BLG, but both are possible for other systems such as the quantum spin Hall insulators described by the Bernevig-Hughes-Zhang model [77]. For square-lattice potential modulated BLG, a weak modulation potential always opens up a trivial gap between the first and second conduction minibands. Topological phase transitions do occur when the modulation potential gets strong as shown in Ref. [26], but this is outside the scope of our perturbation theory analysis, and the topological bands in this regime are not as robust and likely require more fine tuning. A more general analysis of topological band inversions in superlattice potential modulated two-dimensional systems as well as construction of lattice models is left for future work.

It was recently shown experimentally that superlattice modulation potentials can also be produced by adjacent moiré materials [50–53]. Twisted hBN bilayers produce a triangular superlattice potential [78] with $\phi = \pi/6$, which according to our phase diagrams in Figs. 2(e) and 3(c) is unfavorable for topological flat bands [79] and QAHI. TMD bilayers, on the other hand, provide more tunability with choice of material combinations and doping densities. Twisted TMD homobilayers [80] provide a honeycomb-lattice moiré potential for Γ -valley holes, and when the honeycomb lattice is filled by doping, the modulation potential for adjacent layers is honeycomb-shaped. The gate-patterning technique provides higher tunability on the shape and strength of the superlattice potential, but at the current stage it is limited to relatively long superlattice periodicities ($\gtrsim 30$ nm), and the fabrication process introduces significant disorder.

It was shown in Ref. [26] that the topological flat band of SL-BLG in the weak modulation regime has nearly ideal quantum geometry, and that the ground state at filling $\nu = 1/3$ is a fractional Chern insulator (FCI). The robustness of the topological flat bands and related valley-polarized QAHI shown in our work suggests that the validity of these results is probably not limited to a special parameter choice, but that similar results are expected over a wide parameter range. Since the formation of FCIs requires spontaneous valley polarization, we expect that observation of FCIs at fractional fillings is likely within the QAHI regions in Fig. 3. A detailed study of FCIs in SL-BLG and related superlattice modulated systems is left for future work.

ACKNOWLEDGMENTS

Y.Z. acknowledges support from Programmable Quantum Materials, an Energy Frontiers Research Center funded by the U.S. Department of Energy (DOE), Office of Science, Basic Energy Sciences (BES), under Award No. DE-SC0019443. Work at Austin was supported by the Department of Energy under Grant No. DE-SC0019481. T.M.R.W. acknowledges support from the SNSF (Postdoc. Mobility No. 203152) and from the NSF (DMR–2308817). J.C. and S.A.A.G. acknowledge support from the Air Force Office of Scientific Research under Grant No. FA9550-20-1-0260. J.C. is partially supported by the A. P. Sloan Foundation through a Sloan Research Fellowship. The Flatiron Institute is a division of the Simons Foundation.

APPENDIX: DETAILS OF HARTREE-FOCK CALCULATIONS

1. Gate-screened Coulomb interactions

In a dual-gated system, the long-range part of the Coulomb interaction is screened. The gate-screened Coulomb interaction is derived by considering image charges on the metallic gates [81]. We take the following form of gate-screened Coulomb interactions:

$$V_{l=l'}(q) = \frac{2\pi e^2 (e^{qd} - e^{-qd_g})(e^{-qd} - e^{-qd_g})}{\epsilon q (1 - e^{-2qd_g})}, \quad (\text{A1})$$

$$V_{l \neq l'}(q) = \frac{2\pi e^2 e^{qd} (e^{-qd} - e^{-qd_g})^2}{\epsilon q (1 - e^{-2qd_g})}, \quad (\text{A2})$$

where d_g is the distance between two gates. In our calculations we take $d_g = 100$ nm.

In systems with anisotropic dielectric environment $\epsilon_{xx} = \epsilon_{yy} \neq \epsilon_{zz}$, the Coulomb potential takes the same functional form but with effective dielectric constant $\epsilon = \sqrt{\epsilon_{xx}\epsilon_{zz}}$ and with all out-of-plane lengths (i.e., d and d_g) rescaled by a factor of $\sqrt{\epsilon_{xx}/\epsilon_{zz}}$. The value of ϵ in Hartree-Fock calculations in similar systems is often taken to be larger than the realistic value of hBN (~ 5) to effectively describe dynamical screening effects [67,70]. The values of ϵ used in the literature [67–70,82–85] range from 5 to around 20. In our calculations we take $\epsilon = 10$, but we note that the precise values of ϵ, d , and d_g do not affect our qualitative results.

2. Computational details

The self-consistent Hartree-Fock calculations are performed on a 5×5 \boldsymbol{k} grid in the mBZ. The momentum-space cutoff is made by keeping three momentum shells (37 \boldsymbol{g} points). The relatively small number of \boldsymbol{k} points is chosen due to the long superlattice periodicity (30–50 nm as compared to ~ 10 nm in moiré systems), and the small \boldsymbol{g} cutoff achieves good convergence because of the weak superlattice potential in our calculations.

- [1] R. Bistritzer and A. H. MacDonald, Moiré bands in twisted double-layer graphene, *Proc. Natl. Acad. Sci. USA* **108**, 12233 (2011).
- [2] Y. Cao, V. Fatemi, A. Demir, S. Fang, S. L. Tomarken, J. Y. Luo, J. D. Sanchez-Yamagishi, K. Watanabe, T. Taniguchi, E. Kaxiras *et al.*, Correlated insulator behaviour at half-filling in magic-angle graphene superlattices, *Nature (London)* **556**, 80 (2018).
- [3] Y. Cao, V. Fatemi, S. Fang, K. Watanabe, T. Taniguchi, E. Kaxiras, and P. Jarillo-Herrero, Unconventional superconductivity in magic-angle graphene superlattices, *Nature (London)* **556**, 43 (2018).
- [4] M. Yankowitz, S. Chen, H. Polshyn, Y. Zhang, K. Watanabe, T. Taniguchi, D. Graf, A. F. Young, and C. R. Dean, Tuning superconductivity in twisted bilayer graphene, *Science* **363**, 1059 (2019).
- [5] M. Serlin, C. Tschirhart, H. Polshyn, Y. Zhang, J. Zhu, K. Watanabe, T. Taniguchi, L. Balents, and A. Young, Intrinsic quantized anomalous Hall effect in a moiré heterostructure, *Science* **367**, 900 (2020).
- [6] Y. Xie, A. T. Pierce, J. M. Park, D. E. Parker, E. Khalaf, P. Ledwith, Y. Cao, S. H. Lee, S. Chen, P. R. Forrester *et al.*, Fractional Chern insulators in magic-angle twisted bilayer graphene, *Nature (London)* **600**, 439 (2021).
- [7] E. Y. Andrei and A. H. MacDonald, Graphene bilayers with a twist, *Nat. Mater.* **19**, 1265 (2020).
- [8] X. Liu, Z. Hao, E. Khalaf, J. Y. Lee, Y. Ronen, H. Yoo, D. Haei Najafabadi, K. Watanabe, T. Taniguchi, A. Vishwanath *et al.*, Tunable spin-polarized correlated states in twisted double bilayer graphene, *Nature (London)* **583**, 221 (2020).
- [9] J. M. Park, Y. Cao, K. Watanabe, T. Taniguchi, and P. Jarillo-Herrero, Tunable strongly coupled superconductivity in magic-angle twisted trilayer graphene, *Nature (London)* **590**, 249 (2021).
- [10] Z. Lu, T. Han, Y. Yao, A. P. Reddy, J. Yang, J. Seo, K. Watanabe, T. Taniguchi, L. Fu, and L. Ju, Fractional quantum anomalous Hall effect in multilayer graphene, *Nature (London)* **626**, 759 (2024).
- [11] F. Wu, T. Lovorn, E. Tutuc, and A. H. MacDonald, Hubbard model physics in transition metal dichalcogenide moiré bands, *Phys. Rev. Lett.* **121**, 026402 (2018).
- [12] F. Wu, T. Lovorn, E. Tutuc, I. Martin, and A. H. MacDonald, Topological insulators in twisted transition metal dichalcogenide homobilayers, *Phys. Rev. Lett.* **122**, 086402 (2019).
- [13] T. Devakul, V. Crépel, Y. Zhang, and L. Fu, Magic in twisted transition metal dichalcogenide bilayers, *Nat. Commun.* **12**, 6730 (2021).
- [14] Y. Tang, L. Li, T. Li, Y. Xu, S. Liu, K. Barmak, K. Watanabe, T. Taniguchi, A. H. MacDonald, J. Shan *et al.*, Simulation of Hubbard model physics in w_{2s}/w_{2s} moiré superlattices, *Nature (London)* **579**, 353 (2020).
- [15] E. C. Regan, D. Wang, C. Jin, M. I. Bakti Utama, B. Gao, X. Wei, S. Zhao, W. Zhao, Z. Zhang, K. Yumigeta *et al.*, Mott and generalized wigner crystal states in WSe_2/WS_2 moiré superlattices, *Nature (London)* **579**, 359 (2020).
- [16] Y. Xu, S. Liu, D. A. Rhodes, K. Watanabe, T. Taniguchi, J. Hone, V. Elser, K. F. Mak, and J. Shan, Correlated insulating states at fractional fillings of moiré superlattices, *Nature (London)* **587**, 214 (2020).
- [17] A. Ghiotto, E.-M. Shih, G. S. Pereira, D. A. Rhodes, B. Kim, J. Zang, A. J. Millis, K. Watanabe, T. Taniguchi, J. C. Hone *et al.*, Quantum criticality in twisted transition metal dichalcogenides, *Nature (London)* **597**, 345 (2021).
- [18] T. Li, S. Jiang, B. Shen, Y. Zhang, L. Li, Z. Tao, T. Devakul, K. Watanabe, T. Taniguchi, L. Fu *et al.*, Quantum anomalous Hall effect from intertwined moiré bands, *Nature (London)* **600**, 641 (2021).
- [19] Z. Tao, B. Shen, S. Jiang, T. Li, L. Li, L. Ma, W. Zhao, J. Hu, K. Pistunova, K. Watanabe *et al.*, Valley-coherent quantum anomalous Hall state in AB-stacked $MoTe_2/WSe_2$ bilayers, *Phys. Rev. X* **14**, 011004 (2024).
- [20] K. F. Mak and J. Shan, Semiconductor moiré materials, *Nat. Nanotechnol.* **17**, 686 (2022).
- [21] Y. Zeng, Z. Xia, K. Kang, J. Zhu, P. Knüppel, C. Vaswani, K. Watanabe, T. Taniguchi, K. F. Mak, and J. Shan, Thermodynamic evidence of fractional Chern insulator in moiré $MoTe_2$, *Nature (London)* **622**, 69 (2023).
- [22] J. Cai, E. Anderson, C. Wang, X. Zhang, X. Liu, W. Holtzmann, Y. Zhang, F. Fan, T. Taniguchi, K. Watanabe *et al.*, Signatures of fractional quantum anomalous Hall states in twisted $MoTe_2$, *Nature (London)* **622**, 63 (2023).
- [23] H. Park, J. Cai, E. Anderson, Y. Zhang, J. Zhu, X. Liu, C. Wang, W. Holtzmann, C. Hu, Z. Liu *et al.*, Observation of fractionally quantized anomalous Hall effect, *Nature (London)* **622**, 74 (2023).
- [24] F. Xu, Z. Sun, T. Jia, C. Liu, C. Xu, C. Li, Y. Gu, K. Watanabe, T. Taniguchi, B. Tong, J. Jia, Z. Shi, S. Jiang, Y. Zhang, X. Liu, and T. Li, Observation of integer and fractional quantum anomalous Hall effects in twisted bilayer $MoTe_2$, *Phys. Rev. X* **13**, 031037 (2023).
- [25] D. M. Kennes, M. Claassen, L. Xian, A. Georges, A. J. Millis, J. Hone, C. R. Dean, D. Basov, A. N. Pasupathy, and A. Rubio, Moiré heterostructures as a condensed-matter quantum simulator, *Nat. Phys.* **17**, 155 (2021).
- [26] S. A. A. Ghorashi, A. Dunbrack, A. Abouelkomsan, J. Sun, X. Du, and J. Cano, Topological and stacked flat bands in bilayer graphene with a superlattice potential, *Phys. Rev. Lett.* **130**, 196201 (2023).
- [27] S. A. A. Ghorashi and J. Cano, Multilayer graphene with a superlattice potential, *Phys. Rev. B* **107**, 195423 (2023).
- [28] V. Crépel, A. Dunbrack, D. Guerci, J. Bonini, and J. Cano, Chiral model of twisted bilayer graphene realized in a monolayer, *Phys. Rev. B* **108**, 075126 (2023).
- [29] Q. Gao, J. Dong, P. Ledwith, D. Parker, and E. Khalaf, Untwisting moiré physics: Almost ideal bands and fractional Chern insulators in periodically strained monolayer graphene, *Phys. Rev. Lett.* **131**, 096401 (2023).
- [30] X. Wan, S. Sarkar, S.-Z. Lin, and K. Sun, Topological exact flat bands in two-dimensional materials under periodic strain, *Phys. Rev. Lett.* **130**, 216401 (2023).
- [31] G. Tarnopolsky, A. J. Kruchkov, and A. Vishwanath, Origin of magic angles in twisted bilayer graphene, *Phys. Rev. Lett.* **122**, 106405 (2019).
- [32] J. Liu, J. Liu, and X. Dai, Pseudo Landau level representation of twisted bilayer graphene: Band topology and implications on the correlated insulating phase, *Phys. Rev. B* **99**, 155415 (2019).
- [33] N. Bultinck, S. Chatterjee, and M. P. Zaletel, Mechanism for anomalous Hall ferromagnetism in twisted bilayer graphene, *Phys. Rev. Lett.* **124**, 166601 (2020).

- [34] P. J. Ledwith, E. Khalaf, and A. Vishwanath, Strong coupling theory of magic-angle graphene: A pedagogical introduction, *Ann. Phys.* **435**, 168646 (2021).
- [35] J. Wang, J. Cano, A. J. Millis, Z. Liu, and B. Yang, Exact Landau level description of geometry and interaction in a flatband, *Phys. Rev. Lett.* **127**, 246403 (2021).
- [36] N. Morales-Durán, N. Wei, J. Shi, and A. H. MacDonald, Magic angles and fractional Chern insulators in twisted homobilayer transition metal dichalcogenides, *Phys. Rev. Lett.* **132**, 096602 (2024).
- [37] E. Khalaf, S. Chatterjee, N. Bultinck, M. P. Zaletel, and A. Vishwanath, Charged skyrmions and topological origin of superconductivity in magic-angle graphene, *Sci. Adv.* **7**, eabf5299 (2021).
- [38] S. Chatterjee, M. Ippoliti, and M. P. Zaletel, Skyrmion superconductivity: DMRG evidence for a topological route to superconductivity, *Phys. Rev. B* **106**, 035421 (2022).
- [39] P. Törmä, S. Peotta, and B. A. Bernevig, Superconductivity, superfluidity and quantum geometry in twisted multilayer systems, *Nat. Rev. Phys.* **4**, 528 (2022).
- [40] C. Forsythe, X. Zhou, K. Watanabe, T. Taniguchi, A. Pasupathy, P. Moon, M. Koshino, P. Kim, and C. R. Dean, Band structure engineering of 2D materials using patterned dielectric superlattices, *Nat. Nanotechnol.* **13**, 566 (2018).
- [41] Y. Li, S. Dietrich, C. Forsythe, T. Taniguchi, K. Watanabe, P. Moon, and C. R. Dean, Anisotropic band flattening in graphene with one-dimensional superlattices, *Nat. Nanotechnol.* **16**, 525 (2021).
- [42] D. Barcons Ruiz, H. Herzig Sheinflux, R. Hoffmann, I. Torre, H. Agarwal, R. K. Kumar, L. Vistoli, T. Taniguchi, K. Watanabe, A. Bachtold, and F. H. L. Koppens, Engineering high quality graphene superlattices via ion milled ultrathin etching masks, *Nat. Commun.* **13**, 6926 (2022).
- [43] J. Sun, S. A. A. Ghorashi, K. Watanabe, T. Taniguchi, F. Camino, J. Cano, and X. Du, Signature of correlated insulator in electric field controlled superlattice, [arXiv:2306.06848](https://arxiv.org/abs/2306.06848).
- [44] S. Wang, D. Scarabelli, L. Du, Y. Y. Kuznetsova, L. N. Pfeiffer, K. W. West, G. C. Gardner, M. J. Manfra, V. Pellegrini, S. J. Wind *et al.*, Observation of Dirac bands in artificial graphene in small-period nanopatterned GaAs quantum wells, *Nat. Nanotechnol.* **13**, 29 (2018).
- [45] D. Q. Wang, Z. Krix, O. P. Sushkov, I. Farrer, D. A. Ritchie, A. R. Hamilton, and O. Klochan, Formation of artificial Fermi surfaces with a triangular superlattice on a conventional two-dimensional electron gas, *Nano Lett.* **23**, 1705 (2023).
- [46] D. Q. Wang, Z. Krix, O. A. Tkachenko, V. A. Tkachenko, C. Chen, I. Farrer, D. A. Ritchie, O. P. Sushkov, A. R. Hamilton, and O. Klochan, Tuning the bandstructure of electrons in a two-dimensional artificial electrostatic crystal in GaAs quantum wells, [arXiv:2402.12769](https://arxiv.org/abs/2402.12769).
- [47] K. Yasuda, X. Wang, K. Watanabe, T. Taniguchi, and P. Jarillo-Herrero, Stacking-engineered ferroelectricity in bilayer boron nitride, *Science* **372**, 1458 (2021).
- [48] M. Vizner Stern, Y. Waschitz, W. Cao, I. Nevo, K. Watanabe, T. Taniguchi, E. Sela, M. Urbakh, O. Hod, and M. Ben Shalom, Interfacial ferroelectricity by van der Waals sliding, *Science* **372**, 1462 (2021).
- [49] X. Wang, K. Yasuda, Y. Zhang, S. Liu, K. Watanabe, T. Taniguchi, J. Hone, L. Fu, and P. Jarillo-Herrero, Interfacial ferroelectricity in rhombohedral-stacked bilayer transition metal dichalcogenides, *Nat. Nanotechnol.* **17**, 367 (2022).
- [50] D. S. Kim, R. C. Dominguez, R. Mayorga-Luna, D. Ye, J. Embley, T. Tan, Y. Ni, Z. Liu, M. Ford, F. Y. Gao *et al.*, Electrostatic moiré potential from twisted hexagonal boron nitride layers, *Nat. Mater.* **23**, 65 (2024).
- [51] Z. Zhang, J. Xie, W. Zhao, R. Qi, C. Sanborn, S. Wang, S. Kahn, K. Watanabe, T. Taniguchi, A. Zettl, M. Crommie, and F. Wang, Engineering correlated insulators in bilayer graphene with a remote Coulomb superlattice, *Nat. Mater.* **23**, 189 (2024).
- [52] J. Gu, J. Zhu, P. Knuppel, K. Watanabe, T. Taniguchi, J. Shan, and K. F. Mak, Remote imprinting of moiré lattices, *Nat. Mater.* **23**, 219 (2024).
- [53] M. He, J. Cai, H. Zheng, E. Seewald, T. Taniguchi, K. Watanabe, J. Yan, M. Yankowitz, A. Pasupathy, W. Yao, and X. Xu, Dynamically tunable moiré exciton Rydberg states in a monolayer semiconductor on twisted bilayer graphene, *Nat. Mater.* **23**, 224 (2024).
- [54] M. Polini, F. Guinea, M. Lewenstein, H. C. Manoharan, and V. Pellegrini, Artificial honeycomb lattices for electrons, atoms and photons, *Nat. Nanotechnol.* **8**, 625 (2013).
- [55] O. P. Sushkov and A. H. Castro Neto, Topological insulating states in laterally patterned ordinary semiconductors, *Phys. Rev. Lett.* **110**, 186601 (2013).
- [56] H. D. Scammell and O. P. Sushkov, Tuning the topological insulator states of artificial graphene, *Phys. Rev. B* **99**, 085419 (2019).
- [57] N. Suri, C. Wang, B. M. Hunt, and D. Xiao, Superlattice engineering of topology in massive Dirac fermions, *Phys. Rev. B* **108**, 155409 (2023).
- [58] T. Tan, A. P. Reddy, L. Fu, and T. Devakul, Designing topology and fractionalization in narrow gap semiconductor films via electrostatic engineering, [arXiv:2402.03085](https://arxiv.org/abs/2402.03085).
- [59] Z. E. Krix and O. P. Sushkov, Patterned bilayer graphene as a tunable strongly correlated system, *Phys. Rev. B* **107**, 165158 (2023).
- [60] T. Li, J. Ingham, and H. D. Scammell, Artificial graphene: Unconventional superconductivity in a honeycomb superlattice, *Phys. Rev. Res.* **2**, 043155 (2020).
- [61] T. Li, M. Geier, J. Ingham, and H. D. Scammell, Higher-order topological superconductivity from repulsive interactions in kagome and honeycomb systems, *2D Mater.* **9**, 015031 (2022).
- [62] H. D. Scammell, J. Ingham, M. Geier, and T. Li, Intrinsic first- and higher-order topological superconductivity in a doped topological insulator, *Phys. Rev. B* **105**, 195149 (2022).
- [63] E. McCann and M. Koshino, The electronic properties of bilayer graphene, *Rep. Prog. Phys.* **76**, 056503 (2013).
- [64] H. Zhou, T. Xie, A. Ghazaryan, T. Holder, J. R. Ehrets, E. M. Spanton, T. Taniguchi, K. Watanabe, E. Berg, M. Serbyn *et al.*, Half- and quarter-metals in rhombohedral trilayer graphene, *Nature (London)* **598**, 429 (2021).
- [65] H. Zhou, L. Holleis, Y. Saito, L. Cohen, W. Huynh, C. L. Patterson, F. Yang, T. Taniguchi, K. Watanabe, and A. F. Young, Isospin magnetism and spin-polarized superconductivity in bernal bilayer graphene, *Science* **375**, 774 (2022).
- [66] A. M. Seiler, F. R. Geisenhof, F. Winterer, K. Watanabe, T. Taniguchi, T. Xu, F. Zhang, and R. T. Weitz, Quantum cascade of correlated phases in trigonally warped bilayer graphene, *Nature (London)* **608**, 298 (2022).

- [67] C. Huang, T. M. R. Wolf, W. Qin, N. Wei, I. V. Blinov, and A. H. MacDonald, Spin and orbital metallic magnetism in rhombohedral trilayer graphene, *Phys. Rev. B* **107**, L121405 (2023).
- [68] Z. Dong, M. Davydova, O. Ogunnaike, and L. Levitov, Isospin- and momentum-polarized orders in bilayer graphene, *Phys. Rev. B* **107**, 075108 (2023).
- [69] M. Xie and S. Das Sarma, Flavor symmetry breaking in spin-orbit coupled bilayer graphene, *Phys. Rev. B* **107**, L201119 (2023).
- [70] J. M. Koh, J. Alicea, and E. Lantagne-Hurtubise, Correlated phases in spin-orbit-coupled rhombohedral trilayer graphene, *Phys. Rev. B* **109**, 035113 (2024).
- [71] H. Rokni and W. Lu, Layer-by-layer insight into electrostatic charge distribution of few-layer graphene, *Sci. Rep.* **7**, 42821 (2017).
- [72] D. Xiao, M.-C. Chang, and Q. Niu, Berry phase effects on electronic properties, *Rev. Mod. Phys.* **82**, 1959 (2010).
- [73] Even though the superlattice potential vanishes, our calculations at filling $\nu = 1$ implicitly assume a carrier density that is commensurate with the superlattice constant L .
- [74] P. G. Silvestrov and P. Recher, Wigner crystal phases in bilayer graphene, *Phys. Rev. B* **95**, 075438 (2017).
- [75] S. Joy and B. Skinner, Wigner crystallization in bernal bilayer graphene, [arXiv:2310.07751](https://arxiv.org/abs/2310.07751).
- [76] Y. Su, H. Li, C. Zhang, K. Sun, and S.-Z. Lin, Massive Dirac fermions in moiré superlattices: A route towards topological flat minibands and correlated topological insulators, *Phys. Rev. Res.* **4**, L032024 (2022).
- [77] B. A. Bernevig, T. L. Hughes, and S.-C. Zhang, Quantum spin Hall effect and topological phase transition in HgTe quantum wells, *Science* **314**, 1757 (2006).
- [78] P. Zhao, C. Xiao, and W. Yao, Universal superlattice potential for 2D materials from twisted interface inside h-BN substrate, *npj 2D Mater. Appl.* **5**, 38 (2021).
- [79] M. Brzezińska and O. V. Yazyev, Flat bands in bilayer graphene induced by proximity with polar *h*-BN superlattices, [arXiv:2305.09749](https://arxiv.org/abs/2305.09749).
- [80] M. Angeli and A. H. MacDonald, Γ valley transition metal dichalcogenide moiré bands, *Proc. Natl. Acad. Sci. USA* **118**, e2021826118 (2021).
- [81] J. Kang and O. Vafek, Non-Abelian Dirac node braiding and near-degeneracy of correlated phases at odd integer filling in magic-angle twisted bilayer graphene, *Phys. Rev. B* **102**, 035161 (2020).
- [82] M. Xie and A. H. MacDonald, Nature of the correlated insulator states in twisted bilayer graphene, *Phys. Rev. Lett.* **124**, 097601 (2020).
- [83] N. Bultinck, E. Khalaf, S. Liu, S. Chatterjee, A. Vishwanath, and M. P. Zaletel, Ground state and hidden symmetry of magic-angle graphene at even integer filling, *Phys. Rev. X* **10**, 031034 (2020).
- [84] G. Wagner, Y. H. Kwan, N. Bultinck, S. H. Simon, and S. A. Parameswaran, Global phase diagram of the normal state of twisted bilayer graphene, *Phys. Rev. Lett.* **128**, 156401 (2022).
- [85] M. Christos, S. Sachdev, and M. S. Scheurer, Correlated insulators, semimetals, and superconductivity in twisted trilayer graphene, *Phys. Rev. X* **12**, 021018 (2022).